Complementary Control by Additives of the Kinetics of Amorphous $CaCO_3$ Mineralization at an Organic Interface: *In-Situ* Synchrotron X-Ray Observations

Elaine DiMasi,[1,*] Seo-Young Kwak,[1] Fairland F. Amos,[2] Matthew J. Olszta,[2,†] Debra Lush,[2,‡] and Laurie B. Gower[2]

[1]*National Synchrotron Light Source Department, Brookhaven National Laboratory, Upton, New York 11973-5000, USA*

[2]*Department of Materials Science and Engineering, University of Florida, Gainesville, Florida 32611, USA*

(Received 4 November 2005; published 27 July 2006)

The kinetics of biomimetic mineralization at a fatty acid monolayer interface have been measured *in situ* by synchrotron x-ray reflectivity. The formation of biologically relevant amorphous calcium carbonate films is affected by soluble macromolecules, supersaturation rate of change, and Mg cations. We find that these solution conditions influence mineral film formation in a complementary fashion. Poly(sodium acrylate) extends the lifetime of metastable amorphous calcium carbonate, solution saturation controls the mineral film growth rate, and Mg cations create a longer induction time. This is the first quantification of potentially competitive biomineralization mechanisms that addresses nucleation and growth of the amorphous mineral phases, which are important in biomineralization.

DOI: 10.1103/PhysRevLett.97.045503 PACS numbers: 61.10.Kw, 81.10.−h, 82.65.+r, 87.68.+z

Biominerals are composite materials formed by living organisms, and they consist of codeposited ceramic and organic assemblies which exhibit submicron architectures and remarkable physical properties [1,2]. The modified growth of mineral particles by organic additives is motivated in large part by the appeal of potentially harnessing the mechanisms of biomineralization to create new nanocomposites [3,4]. Biominerals' nonequilibrium structures are understood to be produced by their associated proteins and polysaccharides. The crystals often form against organic surfaces, while also in the presence of soluble proteins. A simplified model, for example, depicts a mineralized region bounded by an insoluble fatty acid film on the right and an aqueous phase containing biomacromolecules on the left [Fig. 1(b), inset]. If the atom positions are jointly bound between the mineral face and the insoluble film, the composite is considered to be structurally templated. Both structural templating and kinetic control are important, but most studies to date focus on aspects of structural templating. This approach is credible. First, biomineral crystals are often found experimentally to be aligned to an axis or face of an organized organic assembly. Examples are *c*-axis orientations of calcium carbonates in mollusks and eggshells, and of calcium phosphates in bone along prominent organic planes or fibers [1,3]. Since the organic assemblies are stabilized by their organized structures, it is natural to look for corresponding structural features of the mineral crystal faces. A second reason for the interest in structural templating is the appeal from an engineering point of view. Most biological minerals have rich phase equilibria in aqueous solutions, which are drastically affected by the mixtures of biomolecules and cations present in living organisms. Rather than ''solving'' the problem of mineral stability in such multicomponent mixtures, it would be desirable simply to synthesize an appropriate structural template to dictate crystal formation.

However, experimental data from some model systems have not supported the templating concept. For example, it is still widely quoted that fatty acid monolayers on a liquid surface can exert sufficient control over calcium carbonate mineralization to select the vaterite polytype and to orient the *a-b* face against the monolayer [5]. But *in-situ* synchrotron grazing-incidence diffraction failed to identify oriented mineral crystals [6], while time-resolved reflectivity measurements proved that the calcite and vaterite polytypes of $CaCO_3$ could be kinetically selected against fatty acid monolayers with identical structures [7].

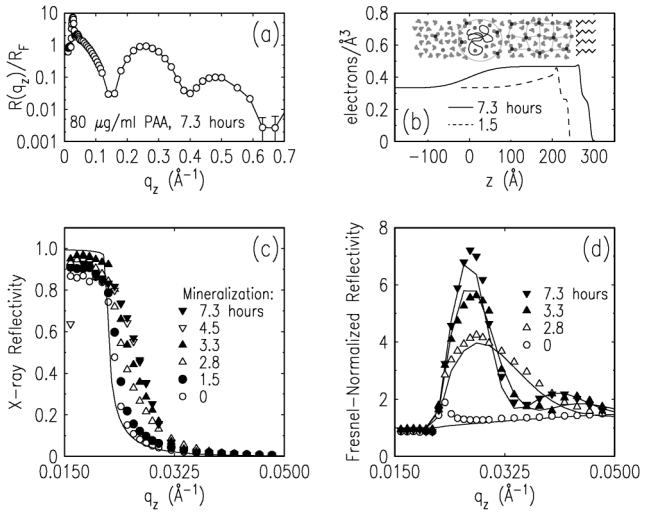

FIG. 1. Representative data from monolayer prepared on 80 μg/ml PAA in subphase. (a) Full R_F-normalized reflectivity data set from sample mineralized for 7.3 hours. (b) Comparison of real-space model profiles for 7.3 and 1.5 hours mineralization. Scheme shows proposed ACC formation process as discussed in the text. (c) Raw reflectivity data time series (symbols), with R_F for comparison (solid line). (d) Selected data from (c) normalized by R_F.

Kinetics, then, is of critical importance for biomimetic mineralization. Unfortunately, time-resolved experimental methods have their own limitations. Atomic force microscopy (AFM) has enabled great strides in determining how growth modifiers like aspartic acid [8] and Mg [9] affect calcite minerals at the atomic scale. But the experiments require flat crystal faces, and give little insight into biologically important amorphous mineral forms. Conversely, x-ray scattering experiments by our group and others [10] have found that the crystallization of $CaCO_3$ often proceeds too quickly for the details to be delineated.

Our approach to the open questions in biomineral kinetics is to focus on amorphous mineral phases. Amorphous calcium carbonate (ACC) is metastable under ambient conditions, but some organisms stabilize this phase in their shells, or take advantage of its malleability to conduct mineral to subcellular compartments, within which it can subsequently crystallize [11]. We have previously shown that polyanionic additives not only stabilize ACC, but maintain sufficient hydration levels to impart the amorphous phase with fluidic character [12]. This has a pronounced impact on the morphologies produced, since the liquid-phase mineral precursor can be molded, extruded in fibers, and infiltrated into organic matrices by capillary forces [13]. In this Letter, we present time-resolved x-ray reflectivity measurements of ACC films formed at fatty acid monolayers in a Langmuir trough, in which solution conditions can be studied systematically. We can detect films as thin as 30 Å and determine their electron densities reliably.

Up to now, proteins, polymers, and Mg^{2+} cations have been referred to interchangeably as ''inhibitors,'' implying that they promote ACC formation simply by inhibiting the nucleation or growth of calcite. In this Letter, for the first time, we show that these kinetic control parameters for ACC film growth are distinct: polyanionic soluble polymers affect film lifetime, saturation rate of change affects film growth rate, and Mg^{2+} content affects induction time. The clear conclusion is that these additives are not interchangeable. Our new approach sets the stage for determining the effects of proteins and solution conditions relevant to biomineralization.

Arachidic acid monolayers were prepared on the surface of a saturated calcium bicarbonate subphase with the following additives: 25–96 μg/ml poly(acrylic acid, sodium salt) (PAA) (molecular weight ~8000), and 0–35 mM Mg^{2+} from $MgCl_2$ dihydrate [14]. Teflon pans having different depths were used in an enclosed trough. In these preparations, escape of CO_2 gas from the subphase raises the degree of supersaturation and precipitates calcium carbonate, according to the overall reaction: $Ca^{2+} + 2HCO_3^- \rightarrow CaCO_3 + H_2O + CO_2$. Depth variation tunes the rate of increase in supersaturation. This process creates mineral films against a single layer of fatty acid molecules, generated from the liquid phase underneath [Fig. 1(b), inset]. The first mineral phase to form is amorphous, observed as a precursor film at the fatty acid monolayer, due to the presence of the PAA; this models the effect of aspartate-rich biomineral-associated proteins. (Essentially identical results are seen when using polyaspartate.) The metastable film will eventually either crystallize or redissolve into solution. In the present work, solutions were prepared with liquid depths of 2.5, 6.5, and 10.0 mm.

X-ray reflectivity was measured at the X22B Liquid Surface Spectrometer, National Synchrotron Light Source, using techniques published previously [14]. Helium flowing through the enclosure protects the film from x-ray damage and maintains a low CO_2 partial pressure at the surface. Data were acquired at 1–2 h intervals following compression of the monolayers. The reflectivity is a measure of the surface-normal structure factor: $R(q_z) \propto R_F(q_z)|\int[\partial\rho(z)/\partial z]e^{-iq_z z}dz|^2$, where $\rho(z)$ is the surface-normal electron density profile, and the Fresnel function R_F is a function of subphase density and absorption coefficient. Oscillations arise from interference of x rays at the monolayer and mineral interfaces, where $\partial\rho(z)/\partial z$ takes nonzero values [Fig. 1(a)]. We model $\rho(z)$ analytically using a series of slabs and Gaussian forms, which represent the film components that build up the electron density profile [Fig. 1(b)]. The signature of mineral film formation occurs at low q_z values, just above the critical wave vector $q_c = 0.022$ Å^{-1}, as shown in the time-dependent low-q_z reflectivity curves in Fig. 1(c). As mineralization proceeds, the data become peaked at $q_z = 0.028$ Å^{-1}, the location of the primary oscillation arising from the buried interface of the thick mineral-rich layer. Because of the steep drop in reflectivity near q_c, the peaked shape of this structure factor is better illustrated by dividing each data set by R_F computed for the water subphase [Fig. 1(d)].

The reflectivity near q_c must be calculated using a matrix method, which includes transmission and reflection of x rays between finely spaced q_z values in a digitized version of the analytic model profile [14]. The essential fit parameters are the mineral film thickness, density, and mineral-subphase interface roughness. Absorption effects have been excluded in the fits presented in this Letter [15]. From our model we quantify the electron density of the mineral film (about 80% that of calcium carbonate hexahydrate), and extract a time-dependent thickness for each sample.

We find, surprisingly, that the polymer concentration affects only the lifetime, and not the growth rate, of the metastable mineral film. The measurements are summarized in Fig. 2(a) and 2(b), which separately show samples with higher and lower PAA concentrations. A growth rate of 75 Å/h is shown in both panels as a guide for the eye. This rate was determined from the 64, 80, and 96 μg/ml PAA data sets. The thickness measurement from the reflectivity is limited at 300 Å by the spectrometer resolution; the longest lived films were visible to the eye as monolithic sheets. With 96 μg/ml PAA, the lifetime of

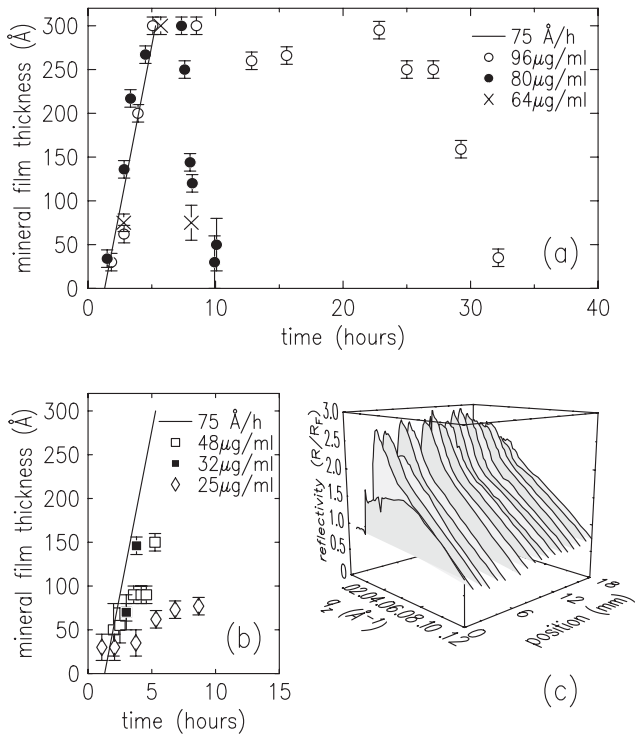

FIG. 2. (a), (b) Time-dependent film thicknesses for all PAA concentrations measured. Subphase depth is 2.5 mm. Line: 75 Å/h guide for the eye. (c) Reflectivity data for a 48 μg/ml sample while translating the beam position through 18 mm on the nonuniform film over a 4 h period.

the film was ≈ 30 hours, after which it uniformly decreased in thickness as it dissolved back into solution. Samples with 64 and 80 μg/ml PAA had the same rate of growth and dissolution, but lifetimes under 10 hours.

Representative thickness data for lower PAA concentrations are shown in Fig. 2(b). These films were unstable. The 32 μg/ml data show two points consistent with 75 Å/h, but other time points showed rough films which could not be analyzed. The 48 μg/ml data were more stable and appear to grow more slowly than 75 Å/h, but by translating the beam position by 1 mm for successive measurements, we observed nonmonotonic variations in thickness [Fig. 2(c)]. For 25 μg/ml the sample was also simultaneously growing and dissolving in patches, able to thicken only to 80 Å and last <9 h. Thus, the polymer concentration cannot be used to tune the growth rate. Instead, sufficient polymers must be present to stabilize the film, while other factors control growth rate, as we show next.

Since gas escape limits the growth rate for the above system, we explored the effect of the trough depth for constant PAA concentration. The results are shown in Fig. 3(a) for 32 and 96 μg/ml PAA samples. When the depth is increased to 6.5 mm, the film growth rate drops from 75 to 20 Å/h. The 20 Å/h rate is also observed with a further depth increase to 10.0 mm. This dependence of the film growth rate is evocative of the "film" model of

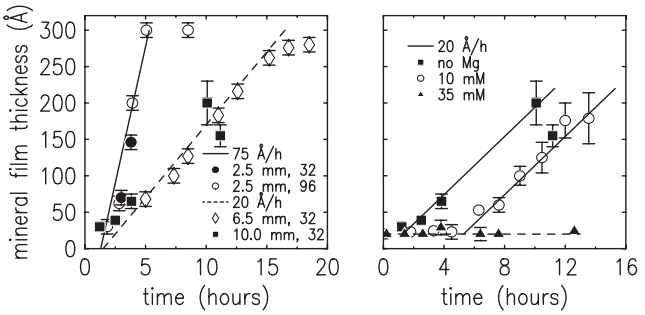

FIG. 3. (a) Time-dependent film thickness of 32 or 96 μg/ml PAA samples for different trough depths. (b) Time-dependent film thickness of 32 μg/ml PAA samples for 0, 10 mM, and 35 mM Mg^{2+} concentrations. The 20 Å/h growth rates (−) are four hours apart. The 20 Å thickness baseline (- - -) is a limit on the film thickness parameter from the reflectivity fits in the absence of a mineral film.

diffusive transport through a stagnant boundary layer of depth $\delta = D/\kappa$, where D is the diffusion coefficient and κ is a mass transport coefficient. Beneath the boundary layer, which supports a linear concentration gradient, the liquid is presumed to be well mixed and has the bulk concentration. Since δ is typically of order 10–100 μm, it is a surprising claim that this system behaves as though it has a 6 mm boundary layer. However, mineral accumulates at a slow rate consistent with CO_2 diffusion over several mm. At 20 Å/h, the mineral film (at 80% of the density of crystalline $CaCO_3 \cdot 6H_2O$, known from prior x-ray analysis) incorporates Ca at $\approx 4 \times 10^{-13}$ mol Ca $cm^{-2}\,sec^{-1}$. Since one CO_2 molecule per $CaCO_3$ formula unit is required for the reaction, CO_2 transfer of at least this order is required. Taking the effective mass transport coefficient as $\kappa = [1.6 \times 10^{-5}\ cm^2/s]/[0.6\ cm]$, and the initial CO_2 concentration of 0.035 M from Henry's Law (bubbled into the solution initially at 1 atm), one finds a transport rate of $\approx 10^{-11}$ mol CO_2 $cm^{-2}\,sec^{-1}$. Diminishing this depth by a factor of 3 increases film growth rate by about the same factor. Thus the boundary layer can supply free carbonate to the mineral film even if it is a few mm thick. These observations highlight the importance of concentration gradients for biomineralization, where submicron compartments and very short time scales are involved.

Finally, Mg^{2+} is an important component in biomineralizing systems. Intra- and extra-cellular fluids as well as sea water have high Mg to Ca ratios, which affect ionic strength and the solubility curves for Ca/Mg carbonate minerals. Mg^{2+} has also been explored in the formation of biomimetic amorphous calcium carbonates, both in the presence [13,16] and absence [17,18] of polymer. Mg^{2+} affects the rate of calcite crystallization [19], and it has been implicated in the induction time for ACC formation [20]. We surveyed 10 and 35 mM Mg^{2+} concentrations with 32 μg/ml PAA in the 10 mm deep trough. The time dependences in Fig. 3(b) show that the sole effect of Mg^{2+} is to delay the film formation. The 20 Å/h growth rate is

observed for both 0 and 10 mM Mg^{2+} samples, but the latter film intercept is shifted 4 hours. With 35 mM Mg^{2+}, film growth was prevented for the duration of the available synchrotron beam time. The reflectivity from this sample was a constant fatty acid film structure. Therefore, our data show that Mg^{2+} does not control the rate of accumulation of ACC.

In summary, *in-situ* x-ray reflectivity has distinguished three different kinetic controls over amorphous calcium carbonate mineralization: growth rate depending upon counterion concentration, ACC lifetime enhanced by polyanionic soluble polymers, and determination by Mg^{2+} of an induction time for film formation. These complementary parameters are all important in biomineralization.

Acidic soluble proteins are known to stabilize amorphous biominerals [11]. *In-situ* AFM studies have shown that aspartic acid interferes directly with growth at calcite edge sites [8]. This physical mechanism, which retards the crystallization of calcite, could play a role in allowing metastable ACC to form, but in this case one would expect macromolecule concentrations to dominate the kinetics. It has also been proposed that macromolecules can be occluded within biominerals, and play a more chemical role in their stability [21]. Our data appear to be compatible with this scenario, since we show that greater PAA concentration extends film life and that for a given polymer concentration, the rate of accumulation of mineral is controlled by other parameters. However, our experience with the polymer-induced liquid-precursor process, in which the polymer drives mineralization by creating a mineral-rich liquid phase which separates from the dilute solution, has suggested that the polymer's role is to sequester cations, which can be later released at a greater rate where counterions are present [12,13]. In the present experiment, the proposed mechanism is shown in the scheme in Fig. 1(b). Against the fatty acid monolayer, a region of amorphous calcium carbonate forms, comparable to but more hydrated than calcium carbonate hexahydrate. The mineral is generated from a more diffuse layer beneath it, where the PAA (shown as black folded curve) has collected Ca^{2+} cations. The new phase is formed when the critical concentration of CO_3^{2-} species becomes available. This is why the mineral formation rate is not influenced by PAA concentration: instead, the counterion is the limiting reagent, which for this reaction chamber is determined by the gas escape rate. The effect of Mg^{2+} is then explained not by competition at $CaCO_3$ surfaces as other studies have addressed, but by competition with Ca^{2+} for proximity to the charged polymer. Eventually, some Mg^{2+} will exchange with Ca^{2+} since PAA has a greater affinity for Ca^{2+} and Mg^{2+} is more strongly solvated than Ca^{2+}. Hence, the Mg^{2+} delays the accumulation of a critical concentration of Ca^{2+} in the PAA/cation complex which supplies the mineral phase. In biomineralization, where an organism must tune cation and counterion concentrations precisely in both position and time, the joint controls of acidic polypeptides and Mg^{2+} may cooperate in the same way. Future work will address the relationship between these transient effects and the crystallization process.

This work is supported by USDOE Contract No. DE-AC02-CH10886 at BNL and by NSF No. DMR-0094209, NSF No. EEC-94-02989, and NIH No. R01 DK59765-01 at U. Florida.

*Corresponding author.
Email address: dimasi@bnl.gov
†Present address: Penn State University, University Park, PA, USA.
‡Present address: Pompano Beach, FL, USA.

[1] S. Weiner and L. Addadi, J. Mater. Chem. **7**, 689 (1997).
[2] E. Bäuerlein, Angew. Chem. **42**, 614 (2003).
[3] N. Dan, Trends Biotechnol. **18**, 370 (2000).
[4] C. Li and D. L. Kaplan, Curr. Opin. Solid State Mater. Sci. **7**, 265 (2003).
[5] B. R. Heywood, S. Rajam, and S. Mann, J. Chem. Soc., Faraday Trans. **87**, 735 (1991).
[6] J. Kmetko, C. Yu, G. Evmenenko, S. Kewalramani, and P. Dutta, Phys. Rev. B **68**, 085415 (2003).
[7] E. DiMasi, M. J. Olszta, V. M. Patel, and L. B. Gower, Cryst. Eng. Comm. **5**, 346 (2003).
[8] C. A. Orme, A. Noy, A. Wierzbicki, M. T. McBride, M. Grantham, H. H. Teng, P. M. Dove, and J. J. De Yoreo, Nature (London) **411**, 775 (2001).
[9] K. J. Davis, P. M. Dove, L. E. Wasylenski, and J. J. De Yoreo, Am. Mineral. **89**, 714 (2004).
[10] D. Pontoni, J. Bolze, N. Dingenouts, T. Narayanan, and M. Baullauff, J. Phys. Chem. B **107**, 5123 (2003).
[11] L. Addadi, S. Raz, and S. Weiner, Adv. Mater. **15**, 959 (2003).
[12] L. B. Gower and D. J. Odom, J. Cryst. Growth **210**, 719 (2000).
[13] M. J. Olszta, D. J. Odom, E. P. Douglas, and L. B. Gower, Connective Tissue Research **44**, 326 (2003).
[14] E. DiMasi, V. M. Patel, M. Sivakumar, M. J. Olszta, Y. P. Yang, and L. B. Gower, Langmuir **18**, 8902 (2002).
[15] See EPAPS Document No. E-PRLTAO-97-036631 for the method used to incorporate absorption terms in the matrix method calculations for modeling the reflectivity data. For more information on EPAPS, see http://www.aip.org/pubservs/epaps.html.
[16] S. Raz, S. Weiner, and L. Addadi, Adv. Mater. **12**, 38 (2000).
[17] Y.-J. Han, L. M. Wysocki, M. S. Thanawala, T. Siegrist, and J. Aizenberg, Angew. Chem. **117**, 2438 (2005).
[18] S.-Y. Kwak, E. DiMasi, Y.-J. Han, J. Aizenberg, and I. Kuzmenko, Crystal Growth and Design **5**, 2139 (2005).
[19] Y. Zhang and R. A. Dawe, Chem. Geol. **163**, 129 (2000).
[20] E. Loste, R. M. Wilson, R. Seshadri, and F. C. Meldrum, J. Cryst. Growth **254**, 206 (2003).
[21] J. Aizenberg, J. Hanson, T. F. Koetzle, S. Weiner, and L. Addadi, J. Am. Chem. Soc. **119**, 881 (1997).

Complementary control by additives of the kinetics of amorphous $CaCO_3$ mineralization at an organic interface: effect of absorption corrections on the modeling of in-situ x-ray reflectivity data

Elaine DiMasi* and Seo-Young Kwak

National Synchrotron Light Source Dept.,

Brookhaven National Laboratory, Upton NY 11973-5000

Fairland F. Amos, Matthew J. Olszta,† Debra Lush,‡ and Laurie B. Gower

Department of Materials Science and Engineering,

University of Florida, Gainesville FL 32611

*Corresponding author: dimasi@bnl.gov

†Present address: Penn State Univ., University Park, PA

‡Present address: Pompano Beach, FL

In previous reports [1] we explicitly disregarded the effects of absorption of x-rays at the interfaces between regions of differing electron density. In reality the index of refraction of x-rays in a medium is a complex quantity: $n = 1-\delta-i\beta$, where $\delta \cong r_0\lambda^2\rho/(2\pi)$ is equivalent to the electron density ρ, and β is the absorption term, sometimes written in the form of an absorption length $\mu = \lambda/4\pi\beta$. Our studies describe films of unknown composition; though we can presume that the mineral underlayer contains a mixture of calcium carbonate and water, we need not know the relative proportions of the two components to fit the data with an effective electron density ρ. The β term on the other hand strongly depends on both the scattering species and the density. Modeling β properly requires additional parameters for various scattering species, and furthermore each β must be scaled in a physical way with the corresponding δ values. Furthermore, these might co-vary with parameters such as interface roughnesses in a way that makes unique fits difficult to obtain, since all the structural information comes from one low-q_z oscillation which is rather quickly damped.

Still, absorption is not obviously negligible at low q_z for the thickest films, since the x-rays enter the film at near-grazing angles of 0.2° and travel 10-20 μm to reach the buried interface and return to the surface. To quantify the effects of absorption, we studied simplified models consiting of only one "mineral" adlayer on a "water" subphase. For water, the literature value $\beta = 1.25(10)^{-8}$ ($\mu = 0.098$ cm) was used to describe the subphase. For the "mineral" layer, we combine our best-fit experimental electron density value ($\rho_M = 1.4 \times \rho_{\mathrm{H_2O}}$) with an absorption parameter calculated in an independent-atom algorithm available online from the Lawrence Berkeley Laboratory Center for X-ray Optics. The value of $\beta = 9.35(10)^{-8}$ ($\mu = 0.013$ cm) was determined from the known composition and density of crystalline calcium carbonate hexahydrate. This is an overestimate of β since our films are less dense than $CaCO_3 \cdot 6H_2O$.

The matrix calculation is achieved by modeling the system as a series of layers of differing refraction index, and writing coupled wave equations for surface-normal x-rays with their boundary conditions across the interface between layers n and $(n+1)$ [2]:

$$\psi = A\exp(ikz) + B\exp(-ikz)\ ,$$

and at z_n, $\psi_n = \psi_{n+1}$ and $d(\psi_n)/dz = d(\psi_{n+1})/dz$, so that

$$A_n\exp(ik_nz_n) + B_n\exp(-ik_nz_n) = A_{n+1}\exp(ik_{n+1}z_n) + B_{n+1}\exp(-ik_{n+1}z_n)$$

and

$$A_n k_n \exp(ik_n z_n) - B_n k_n \exp(-ik_n z_n) = A_{n+1} k_{n+1} \exp(ik_{n+1} z_n) - B_{n+1} k_{n+1} \exp(-ik_{n+1} z_n) \; .$$

This defines the matrix M_n relating the coefficients across the boundary located at z_n:

$$\begin{pmatrix} A_{n+1} \\ B_{n+1} \end{pmatrix} = \begin{pmatrix} \frac{1}{2}\left(1+\frac{q_n}{q_{n+1}}\right)\exp\left[-i\left(q_n - q_{n+1}\right)z_n/2\right] & \frac{1}{2}\left(1-\frac{q_n}{q_{n+1}}\right)\exp\left[+i\left(q_n + q_{n+1}\right)z_n/2\right] \\ \frac{1}{2}\left(1-\frac{q_n}{q_{n+1}}\right)\exp\left[-i\left(q_n + q_{n+1}\right)z_n/2\right] & \frac{1}{2}\left(1+\frac{q_n}{q_{n+1}}\right)\exp\left[+i\left(q_n - q_{n+1}\right)z_n/2\right] \end{pmatrix} \begin{pmatrix} A_n \\ B_n \end{pmatrix}$$

where we have replaced k_n with $(-q_n/2)$ to correspond to our dependent variable in the reflectivity, $q_z = -2k_z$. Otherwise this is equivalent to equation (6) in Ref. [2] except for a typographical error in that reference (sign in exponent in $M_{21,n}$).

The values of $q_n = (4\pi/\lambda) n_n \sin\theta_n$ in the refracting layers may be related to the incident wavevector $q_z = (4\pi/\lambda)\sin(\theta_0)$, with θ_0 the incident angle at the air interface [3]. From Snell's Law, $\cos(\theta_0) = n_1\cos(\theta_1) = n_2\cos(\theta_2) = \ldots = n_N\cos(\theta_N)$ for all interfaces. We use $n_n = 1 - \delta_n - i\beta_n$, the small-angle approximation, and the relationship between δ, the electron density ρ_n of each layer relative to the subphase density, and the critical angle $q_c = \sqrt{2\delta_{\mathrm{H_2O}}}$:

$$n_n \sin\theta_n = \sqrt{n_n^2\left(1-\cos^2\theta_n\right)} = \sqrt{n_n^2 - \cos^2(\theta_0)} = \sqrt{\sin^2(\theta_0) - 2\delta_n - 2i\beta_n} \; ;$$

$$q_n = (4\pi/\lambda) n_n \sin\theta_n = \sqrt{(q_z)^2 - \rho_n q_c^2 - (32\pi^2/\lambda^2) i\beta_n} \; .$$

$$\Re\{q_n\} = \frac{1}{\sqrt{2}}\left[\left[\left(q_z^2 - \rho_n q_c^2\right)^2 + \left(32\pi^2\beta_n/\lambda^2\right)^2\right]^{1/2} + \left(q_z^2 - \rho_n q_c^2\right)\right]^{1/2}$$

and

$$\Im\{q_n\} = \frac{-1}{\sqrt{2}}\left[\left[\left(q_z^2 - \rho_n q_c^2\right)^2 + \left(32\pi^2\beta_n/\lambda^2\right)^2\right]^{1/2} - \left(q_z^2 - \rho_n q_c^2\right)\right]^{1/2} \; .$$

This is equivalent to the equations between Eq.(5) and (6) in Ref. [3] except that a typographical error (missing square brackets) makes the final power (1/2) ambiguous in that reference. In our previous publication, these expressions with $\beta_n \equiv 0$ were used, so that all q_n were strictly real, and the fit parameters within the computation comes from the parameterization of $\rho(z)$ as a series of ρ_n terms.

The reflectivity is obtained by calculating $M = M_N M_{N-1} \cdots M_2 M_1 M_0$ for all layers including the last, which is the subphase, from which it is assumed that no further reflection occurs. The reflected intensity is the magnitude of the ratio of amplitudes incident and reflected from the surface, or $R(q_z) = \left|\left(\frac{m_{21}}{m_{22}}\right)\left(\frac{m_{21}}{m_{22}}\right)^*\right|$ [2–4].

In our investigation we computed the reflectivity of a model film as described above. It was necessary to smoothly vary the adlayer β to the value of the subphase in order to avoid spurious reflections from the mathematical "layers" extending beyond the film (i.e., beyond the region where $\rho(z)$ was modeled as varying). With mineral parameters $\beta_M = 9.35(10)^{-8}$, $\rho_M = 1.4 \times \rho_{\mathrm{H_2O}}$, film thickness 300 Å, and buried-interface roughness $\sigma = 80$ Å, our algorithm used:

$$\rho(z) < 1 : \beta = 0$$
$$\rho(z) = 1 : \beta = \beta_{\mathrm{H_2O}} = 1.25(10)^{-8}$$
$$\rho(z) > 1 : \beta = \beta_{\mathrm{H_2O}} + \left[\frac{\beta_M - \beta_{\mathrm{H_2O}}}{\rho_M - 1}\right](\rho(z) - 1)$$

This linear variation is a bit unphysical, but not significantly so. We found that the difference between setting $\beta = 0$ and $\beta = \beta_{\mathrm{H_2O}}$ was almost undetectable. In the figure below, we show a model Fresnel-normalized reflectivity computed with the parameters specified above, including absorption (open circles). This data set was then fit with $\beta_M = \beta_{\mathrm{H_2O}}$ fixed. (This is equivalent to neglecting absorption since we found no difference between calculations with $\beta_M = 0$ versus $\beta_M = \beta_{\mathrm{H_2O}}$.) The fit curve (solid line) results in these parameters: $\rho_M = 1.403 \times \rho_{\mathrm{H_2O}}$, film thickness 304 Å, and buried-interface roughness $\sigma = 75.8$ Å. The changes from the input values are insignificant, demonstrating that absorption effects are not important in our study.

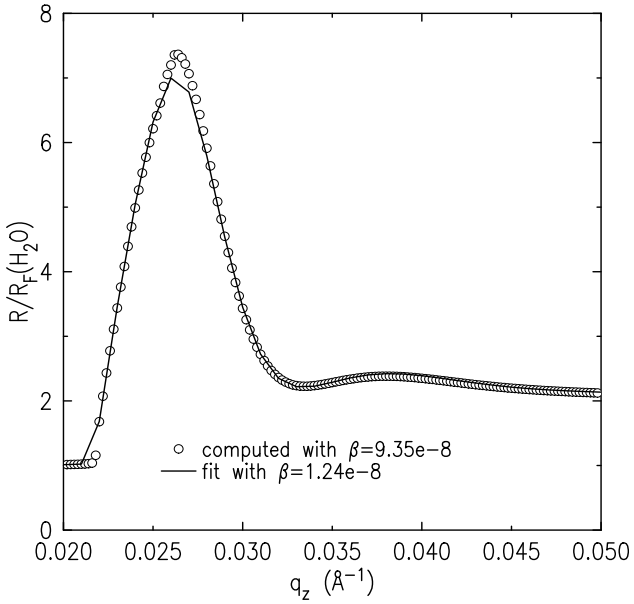

Acknowledgments

The authors gratefully acknowledge Dr. Masafumi Fukuto of Brookhaven National Laboratory for helpful discussions of this analysis. This work is supported by USDOE Contract DE-AC02-CH10886 at BNL and by NSF DMR-0094209, NSF EEC-94-02989, and NIH R01 DK59765-01 at U. Florida.

---

[1] E. DiMasi, V. M. Patel, M. Sivakumar, M. J. Olszta, Y. P. Yang, and L. B. Gower, Langmuir **18**, 8902 (2002).

[2] J. Lekner, *Developments in Electromagnetic Theory and Applications, No. 3* (Martinus Nijhoff, Dodrecht, 1987), chap. 12.

[3] L. G. Parratt, Phys. Rev. **95**, 359 (1954).

[4] A. Gibaud, *X-Ray and Neutron Reflectivity: Principles and Applications* (Springer-Verlag, 1999), chap. 3, pp. 99–120.